

# Anomalous carrier dynamics and localization effects in nonpolar $m$ -plane InGaN/GaN quantum wells at high temperatures

Xuanqi Huang<sup>a,\*</sup>, Dongying Li<sup>a</sup>, Po-Yi Su<sup>b</sup>, Houqiang Fu<sup>a</sup>, Hong Chen<sup>a</sup>, Chen Yang<sup>a</sup>, Jingan Zhou<sup>a</sup>, Xin Qi<sup>a</sup>, Tsung-Han Yang<sup>a</sup>, Jossue Montes<sup>a</sup>, Xuguang Deng<sup>a</sup>, Kai Fu<sup>a</sup>, Steven P. DenBaars<sup>c</sup>, Shuji Nakamura<sup>c</sup>, Fernando A. Ponce<sup>b</sup>, Cun-Zheng Ning<sup>a</sup>, Yuji Zhao<sup>a,\*\*</sup>

<sup>a</sup> School of Electrical, Computer and Energy Engineering, Arizona State University, Tempe, AZ, 85287, USA

<sup>b</sup> Department of Physics, Arizona State University, Tempe, AZ, 85287, USA

<sup>c</sup> Materials Department, University of California, Santa Barbara, CA, 93106, USA

## ARTICLE INFO

### Keywords:

Carrier dynamics  
Localization  
InGaN  
Quantum wells  
High temperature

## ABSTRACT

Nonpolar InGaN/GaN quantum wells (QWs) have gained significance for efficient light emitting since it eliminates polarization-related effects and allows for higher radiative capability. Although much progress has been made in analyzing carrier localization effects at cryogenic temperatures, carrier dynamics at above room temperatures are still not well understood. In this work, we have observed and explored anomalous carrier dynamics of two nonpolar  $m$ -plane InGaN/GaN QWs at high temperatures by combining scanning transmission electron microscopy (STEM) and photophysical characterization. Both experimental and theoretical results suggest that carrier lifetime in both samples increases with temperature in a certain range of temperature. However, the reduced integrity and uniformity of QWs make carriers more prone to the nonradiative Shockley-Reed-Hall recombination as temperature rises. Moreover, both acoustic and optical phonon scatterings dominate from 300 to 600 K through the analysis on the evolution of photoluminescence spectra. Overall, these detailed studies provide insights into approaches to evaluate carrier dynamics at elevated temperatures and improve emitting performance to further push the practical efficiency limit.

## 1. Introduction

Recent advances in III-nitrides are poised to radically alter the design and implementation of optoelectronics [1–8] and electronics [9–12]. In recent years, there has been tremendous progress in realizing nonpolar III-nitrides light-emitting-diodes (LEDs) [13,14] and laser diodes (LDs) [15,16]. In addition, novel devices and applications based on nonpolar III-nitrides are now emerging. Nonpolar InGaN solar cells exhibit improved carrier collection efficiency compared to  $c$ -plane counterparts [17] and deliver increased carrier lifetime and enhanced performance at elevated temperatures [18]. Another notable recent example is the vertical  $m$ -plane GaN  $p$ - $n$  diodes that potentially leads to advanced vertical selective-area-doped power devices [19,20].

This ongoing interest in nonpolar III-nitrides structures has been driven by their favorable properties, such as elimination of detrimental polarization-related effects, enhanced radiative recombination and high

degree of polarized luminescence [21,22]. Conventional polar  $c$ -plane III-nitride quantum wells (QWs) based emitters are currently constrained by the strong polarization-induced electric fields, inducing the tilted energy band profile and compromised radiative efficiency. To address this challenge, nonpolar crystal orientation of III-nitrides has been intensively researched for light-emitting applications. Several studies proposed that thick QWs and large active region in nonpolar structures can be employed to further exploit the advantage of high overlap of electron and hole wavefunction in nonpolar QWs [2,23,24]. Others pointed out that excitonic recombination is dominant in nonpolar InGaN QW at room temperature while radiative lifetime in polar QW depends on the injected carrier density [23,25,26]. Theoretical studies also revealed that in nonpolar InGaN QWs, localization of holes originates from indium alloy fluctuation while electrons are tightly bound to holes via coulomb interaction [27,28]. Furthermore, strong localization effects in hole wavefunction, rather than the electron

\* Corresponding author.

\*\* Corresponding author.

E-mail addresses: [xuanqi.huang@asu.edu](mailto:xuanqi.huang@asu.edu) (X. Huang), [yuji.zhao@asu.edu](mailto:yuji.zhao@asu.edu) (Y. Zhao).

wavefunction, explicitly accounts for the inhomogeneous broadening of emission energy of QWs. This difference is attributed to the small localization length of holes compared to electrons [28,29].

Despite the rapid progress in the field, there are significant challenges that remain before the realization of full potential of nonpolar III-nitrides. Therefore, it's imperative to investigate carrier dynamics inside nonpolar QWs at both cryogenic and elevated temperatures. Numerous studies of carrier localization effect at cryogenic temperatures have been reported [25,26,28,30–32], but very few reports exist on the analysis of carrier dynamics above room temperatures. In this study, we have experimentally and theoretically investigated the carrier localization and its impact on carrier dynamics on nonpolar *m*-plane InGaN/GaN QWs at elevated temperatures. Photophysical characterizations combined with high-resolution scanning transmission electron microscopy (STEM) and theoretical modeling suggest that the lack of integrity and uniformity in QWs significantly impact carrier confinement and localization, thus making carriers more prone to nonradiative recombination. In addition, analysis on exciton-phonon scattering mechanisms reveals that both acoustic and optical phonon scatterings dominate in the temperature range of 300–600 K. These detailed results and analysis provide substantial understanding toward improving the optoelectronic performance of III-nitrides.

## 2. Results and discussion

Two InGaN/GaN MQW on nonpolar *m*-plane substrates were grown by conventional metal-organic chemical vapor deposition (MOCVD). The main difference between 2 samples lies in the well thickness, one with a nominal 6-nm InGaN QW and the other one with a 3-nm QW. A more detailed description for these two samples can be found in the 4. Method section. Fig. 1 present the cross-sectional high-angle annular dark-field (HAADF) images of two nonpolar *m*-plane InGaN/GaN MQW samples taken along  $[11\bar{2}0]$  zone axis, which are denoted as *m6* and *m3*, respectively. The sharper and better-defined interfaces of QWs of sample *m6* can be observed in Fig. 1(a) and (b) compared to those of *m3* in Fig. 1

(c) and (d). The QW interfaces are also spatially resolved for *m6* in the intensity profile mapping in the Supplementary Fig. S1(c) due to the Z-contrast nature of STEM-HAADF images. On the contrary in Fig. S1 (f) and (g), long Indium distribution tail in GaN barrier layers (upper interfaces) can be observed, which resembles the graded InGaN/GaN QWs. From Figs. S1(a) and (e), the average thicknesses of one period of InGaN QW and GaN barrier are approximately 18 nm for *m6* and 15 nm for *m3*, respectively. We can therefore conclude that structural uniformity is better preserved in sample *m6* rather than *m3*. Consequently, the potential fluctuation in *m6* are most likely to be induced from QW thickness fluctuation as evidenced in Figs. S1(a–d), while the indium compositional fluctuation mainly accounts for potential fluctuation in *m3*, assuming similar random alloy disorder and strain in both samples. In addition, it's also worth noting that the interface of InGaN/GaN layers [upper interfaces, see Fig. 1(b) and (d)] is generally sharper than that of GaN/InGaN layers [lower interfaces, see Fig. 1(a) and (c)]. This phenomenon has also been observed in previous reports on InGaN/GaN QWs [28,33,34], and is typically known as compositional pulling effect [35]. The details of the epitaxial growth and fabrication processes for two nonpolar *m*-plane InGaN/GaN MQW structures can be found in 4. Method section.

The excitation power-dependent PL and TRPL measurements have been widely adopted to investigate the underlying recombination process and the corresponding carrier dynamics in III-nitride emitters [25, 36,37]. Fig. 2 illustrate the (a) integrated PL intensity and (b) effective carrier lifetime extracted from TRPL at room temperature as a function of excitation laser power for sample *m6* (blue) and *m3* (purple), respectively. The decay curves of power-dependent time-resolved photoluminescence (TRPL) are shown in Fig. S3. Generally, the integrated PL intensity (*I*) is proportional to the excitation power (*P*), i.e., optically injected carrier density, and can be given by  $I \propto P^n$ , where *n* is an indicator of radiative or nonradiative recombination mechanism. In Fig. 2 (a), the values of *n* for both *m6* and *m3* are approaching 1.18 which is larger than 1, suggesting the co-existing radiative and Shockley–Read–Hall recombination in both samples in the range of excitation power employed in our study. Nonetheless, 2 samples exhibit distinct carrier dynamics under laser excitation, even though they share similar effective lifetime at weak excitation. In Fig. 2 (b), the effective lifetime in *m6* keeps reducing until excitation power around 10  $\mu$ W and remains almost constant afterwards. This tendency of unchanged carrier lifetime has been reported previously on both nonpolar *m*-plane [33] and polar *c*-plane [36] InGaN/GaN QWs. We attribute this decreasing lifetime of *m6* to band filling effect of localized centers and higher energy levels rather than the Coulomb screening of the internal electric field in QWs, due to the elimination of internal intrinsic electric field in *m*-plane QWs. Regarding the saturation of the effective lifetime after  $\sim 10 \mu$ W, it can be ascribed to the fully occupied higher energy levels and a wholly excitonic recombination mechanism, which has been previously reported [23]. In comparison, the effective lifetime in *m3* tends to increase up to excitation power around 10  $\mu$ W and then the rising rate slows down. This can be accounted by the gradual quenching of nonradiative recombination centers with more optically injected carriers. Overall, 2 samples exhibit drastically different behavior of carrier lifetime even though sharing similar lifetime under low excitation condition.

To gain more insights into the impact of structural uniformity and carrier localization on carrier dynamics, we have carried out temperature-dependent time-resolved photoluminescence (TRPL) measurements. They are measured at 3 different excitation powers of 1  $\mu$ W, 5  $\mu$ W and 50  $\mu$ W, which correspond to an estimated excited carrier density of  $3 \times 10^{12} \text{cm}^{-3}$ ,  $1 \times 10^{13} \text{cm}^{-3}$  and  $1 \times 10^{14} \text{cm}^{-3}$ , respectively. The PL effective lifetime  $\tau_{\text{eff}}$  under each temperature and excitation power was extracted from each PL decay curve with the fast decay in a biexponential decay function, which is also shown in Fig. S4. The temperature-dependent time-resolved TRPL measurements of sample *m6* and *m3* in range of 20–400 °C and at three different excitation power (1, 5 and 50  $\mu$ W) are shown in the Supplementary Fig. S3. In Fig. 3 (a),

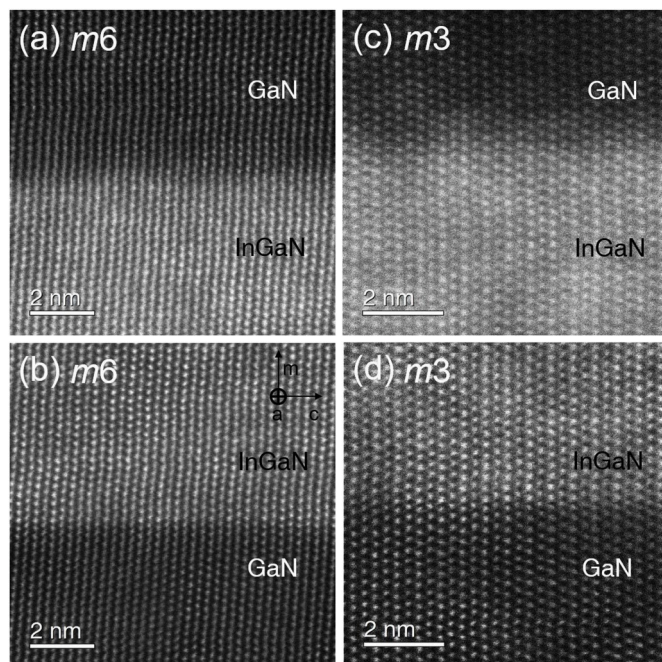
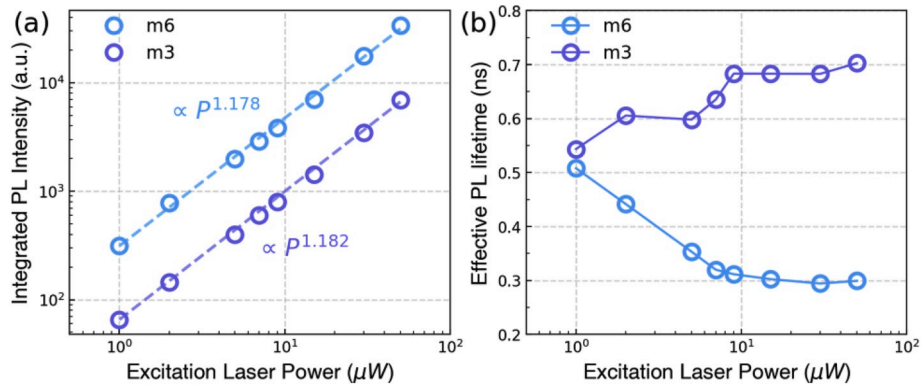


Fig. 1. STEM-HAADF images of interfaces of InGaN/GaN QWs in the atomic-scale for (a–b) sample *m6* and (c–d) *m3*, respectively. (a) and (c) explicitly display the upper GaN/InGaN interfaces while (b) and (d) for lower InGaN/GaN interfaces. Both upper and lower interfaces of InGaN/GaN QWs of *m6* are much sharper than those of *m3*.



**Fig. 2.** (a) Integrated PL intensity and (b) effective carrier lifetime extracted from TRPL measured at room temperature as a function of excitation laser power for m6 (blue) and m3 (purple), respectively.

$\tau_{eff}$  in sample m3 tends to increase and then reduce after 150 °C (~420K). In contrast,  $\tau_{eff}$  in sample m6 in Fig. 3 (b) remains almost constant till 200 °C (~470K) and then rises.

The temperature-dependent  $\tau_{eff}$  of each sample was simulated with a theoretical lifetime model that accounts for carrier localization effect [33,38]. This model assumes that the densities of both free and localized excitons keep in steady state. Thus, the effective decay lifetime ( $\tau_{eff}$ ) of excitons in the QW is given by

$$\frac{1}{\tau_{eff}} = \left( \frac{n_{loc}}{\tau_{loc}} + \frac{n_{free}}{\tau_{free}} \right) / (n_{loc} + n_{free}), \quad (1)$$

where  $n_{loc}$  and  $n_{free}$  are localized and free exciton densities, respectively while  $\tau_{free}$  and  $\tau_{loc}$  represent characteristic decay time for localized and free excitons. The ratio between  $n_{loc}$  and  $n_{free}$  is then give via Saha's law [38] by

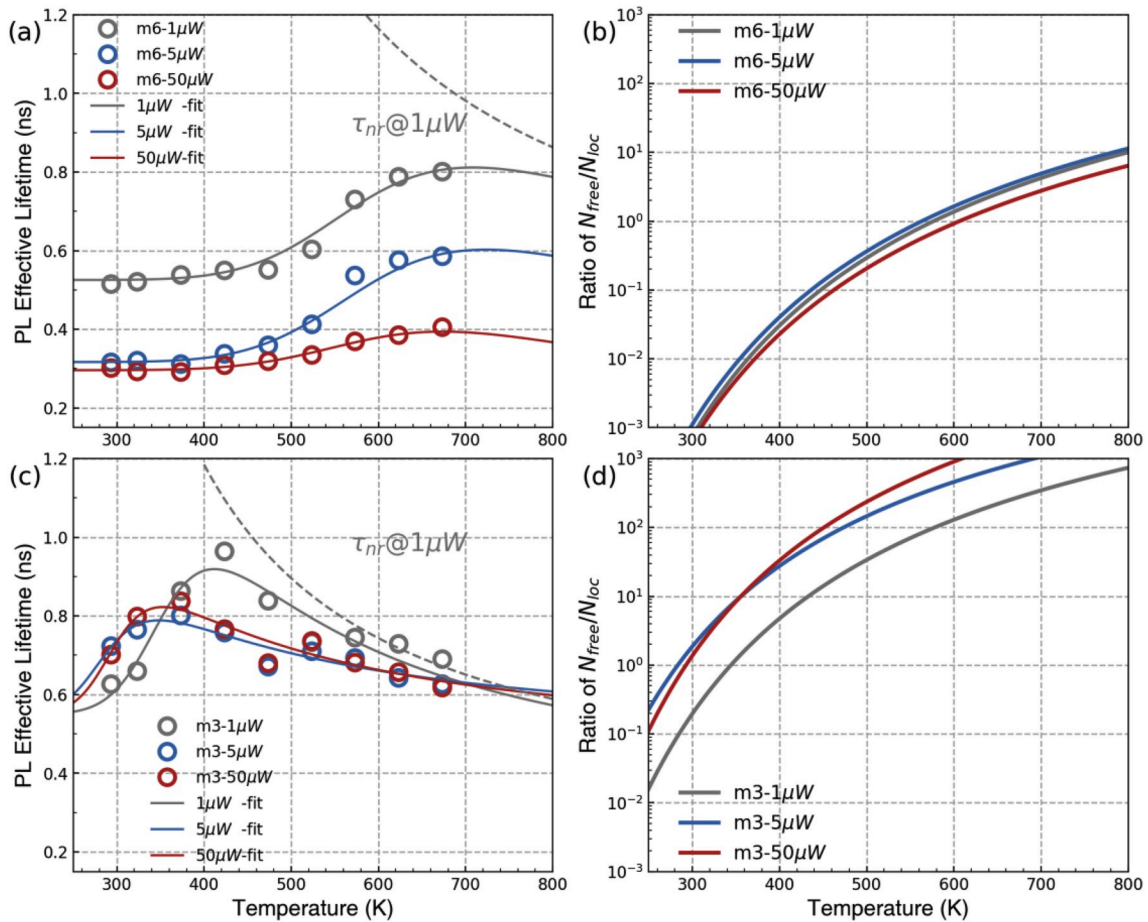


**Fig. 3.** Comparison of carrier dynamics of two *m*-plane InGaN/GaN QW samples. Measured QW effective lifetime (circles) for (a) m6 and (c) m3 at three different excitation powers. Solid lines represent the simulated effective lifetime and the grey dash lines indicate theoretical simulated nonradiative lifetime ( $\tau_{nr}$ ) at 1  $\mu$ W of laser power. Fig. 3(b) and (d) show the ratio of density of free exciton versus localized exciton ( $n_{free}/n_{loc}$ ) deduced from the model for (b) m6 and (d) m3, respectively. In all figures three different excitation powers are plotted with 3 individual colors: grey for 1  $\mu$ W, blue for 5  $\mu$ W and red for 50  $\mu$ W.

$$\frac{n_{free}}{n_{loc}} = \frac{2M_X k_B T}{\pi \hbar^2 N_D} e^{-E_{loc}/k_B T}, \quad (2)$$

where  $M_X$  is the exciton mass,  $E_{loc}$  is the localization energy, and  $N_D$  is the localization center density in QWs. The  $\tau_{loc}$  is considered as temperature-independent due to the fact that it only depends on the coherence volume of localized excitons [39]. In addition, the effective decay lifetime of free exciton ( $\tau_{free}$ ) constitutes of both radiative ( $\tau_r$ ) and nonradiative lifetimes ( $\tau_{nr}$ ):

$$\frac{1}{\tau_{free}} = \frac{1}{\tau_r} + \frac{1}{\tau_{nr}}, \quad (3)$$

The radiative lifetime of free exciton ( $\tau_r$ ) increases linearly with temperature [40] and is given by

$$\tau_r = \frac{6M_X k_B T}{\hbar^2 k_{\parallel}^2} \tau_0, \quad (4)$$

where  $\tau_0$  represents radiative lifetime of free excitons at  $k_{\parallel} = 0$ ,  $k_{\parallel}$  is the in-plane wave vector of free excitons within the light cone. The value of  $\tau_0$  was taken as 10 ps in the simulation [33]. On the other hand, a nonradiative recombination process with a characteristic activation energy  $E_A$  is also taken into account:

$$\tau_{nr} = \tau_{nr0} \cdot e^{-E_A/k_B T} \quad (5)$$

where  $\tau_{nr0}$  is the indication of interaction between excitons and non-radiative recombination centers. Therefore, there are five main parameters for fitting:  $\tau_{loc}$ ,  $E_{loc}$ ,  $N_D$ ,  $\tau_{nr0}$  and  $E_A$ . During the fitting procedure,  $\tau_{loc}$  has been set to match the lifetime around room temperature ( $\sim 300$  K).  $E_{loc}$  and  $N_D$  have been optimized to fit the increasing range of effective lifetime.  $\tau_{nr0}$  and  $E_A$  have been tuned to account for the reduction of the effective lifetime ( $>650$  K for  $m6$  and  $>400$  K for  $m3$ ).

The solid lines in Fig. 3(a) and (c) exhibit the fitting results for 2 samples under 3 excitation power. All fitting parameters are tabulated in Table 1. The grey dashed lines in Fig. 3(a) and (c) represent the non-radiative recombination lifetime at the excitation power of  $1 \mu\text{W}$ , which are plotted for better illustrative purpose. The localization center density  $N_D$  is around  $2 \times 10^{10} \text{cm}^{-2}$  for  $m6$  while approximately  $1 \times 10^8 \text{cm}^{-2}$  for  $m3$ . This parameter obtained from previous reports under cryogenic temperatures is in the range of  $10^{10}$  and  $10^{11} \text{cm}^{-2}$  in AlGaAs/GaAs QW where exciton localization is induced from monolayer variation of well width [41]. Moreover, it's approximately  $1 \times 10^{12} \text{cm}^{-2}$  in  $m$ -plane InGaN/GaN MQW [33], which is within the scale of Indium fluctuation observed from atom probe tomography study [42]. In comparison, localization center density  $N_D$  obtained in our study is at least 2 orders of magnitude lower than the previous reports, which can be treated as deep localization centers in MQWs. This significant difference can be accounted for by the measurement temperature range, thus providing substantial insights into approaches to evaluate emission properties of III-nitride MQW above ambient temperatures in addition to cryogenic studies.

**Table 1**

Parameters determined from fitting lifetime model for  $m6$  and  $m3$  at 3 excitation powers.

	$\tau_{nr0}$ (ns)	$E_A$ (meV)	$N_D (\times 10^8 \text{cm}^{-2})$	$E_{loc}$ (meV)	$\tau_{loc}$ (ns)
$m6 - 1 \mu\text{W}$	0.351	62.0	$2.73 \times 10^2$	352	$0.525^a$
$m6 - 5 \mu\text{W}$	0.218	75.6	$2.80 \times 10^2$	342	$0.316^a$
$m6 - 50 \mu\text{W}$	0.126	77.5	$5.04 \times 10^2$	341	$0.296^a$
$m3 - 1 \mu\text{W}$	0.293	48.2	7.90	$300^a$	$0.55^a$
$m3 - 5 \mu\text{W}$	0.439	23.6	1.10	$300^a$	$0.55^a$
$m3 - 50 \mu\text{W}$	0.433	24.2	1.13	$300^a$	$0.55^a$

<sup>a</sup> The numbers with asterisks (\*) mean that they are fixed in the fitting.

Furthermore, we can also obtain the  $E_{loc}$  of  $\sim 0.34 \text{eV}$  for  $m6$  and  $\sim 0.30 \text{eV}$  for  $m3$ . It's worth noting that they are roughly close to the value of conduction band offsets in each sample, as shown in Fig. S2. We therefore posit that under high temperatures, the major transport mechanism for electron is delocalization via thermal escape from QWs to barriers and then recombine nonradiatively. This is possibly related to the large localization radius of electrons compared to holes [29].

Moreover, the ratio of free and localized carrier densities can be also estimated from this model and plotted in Fig. 3(b) and (d). For  $m6$ ,  $n_{loc}$  and  $n_{free}$  become equal in the range of 550–600K, which corresponds to the temperature where FWHM of PL peaks increases significantly as shown in Fig. 6. In contrast for  $m3$ , free excitons become dominant at around 300K, especially under high excitation conditions. By taking into account of the STEM studies in Fig. 1 and results of excitation-dependent carrier lifetime as shown in Fig. 2(b), we can then propose that the fundamental difference in carrier dynamics of both samples lies in disparate potential confinement of carriers. For  $m3$ , the significant Indium fluctuation across barrier layers contributes to obscure interface between QWs and barriers, diminishing carrier confinement in QWs. This effect further populates carriers more spatially in both QW and barrier regions and more energetically into higher energy levels, which in turn make carriers susceptible to nonradiative centers. Therefore, this accounts for larger  $n_{free}/n_{loc}$  ratio and the decreasing lifetime after 400K observed in  $m3$ . In comparison,  $m6$  acquires explicit and uniform QW/barrier interface and hence better carrier confinement. Therefore carriers stay at localization centers and are able to maintain strong radiative capability, especially considering exciton radius is much smaller than the QW width [43].

Fig. 4(a) and (b) present the streak camera spectroscopy images for two  $m$ -plane samples recorded at RT under identical high excitation power. We observe a much broader emission spectrum of MQW of  $m6$  in Fig. 4(a) compared to that of  $m3$  in Fig. 4(b) at early delays. Then the emission spectra of MQW progressively diminish with increasing time delays in the vicinity of 2.85 eV for  $m6$  and 2.90 eV for  $m3$ .

To further elucidate the evolution of carrier dynamics of both samples, Fig. 4(c) and (d) show the time-resolved spectra extracted from streak images at 4 different time delays. A time interval of 100 ps is chosen for  $m6$  and 300 ps for  $m3$ . The broad and asymmetric emission from MQW at early delays of both samples can be attributed to the phase space filling effect. In addition, a progressive carrier cooling process of exciton is evidenced by the gradual declining slope of the high-energy tail. Moreover, the slight redshift of the peak energy of  $m6$  is observed in Fig. 4(c) while it remains almost constant for  $m3$ . This suggests that only partial localization centers have been saturated under such excitation, which is also consistent with higher localization carrier density estimated from Fig. 3 and the larger FWHM value of  $m6$  at RT in Fig. 5. It's also worth noting that there exists a carrier redistribution process in the range of 2.70–2.90 eV for  $m6$  [see Fig. 4(a) and (c)], which is not observed in  $m3$ . For  $m6$  in the early decay, emission from lower energy centers first rises rapidly (from  $t_0$  to  $t_0+100\text{ps}$ ) and then reduces which resembles the evolution of the emission from the extended states. This result serves as a strong indicator of carrier localization effect in  $m6$  and also reinforces our previous arguments for the temperature-dependent carrier dynamics in Fig. 3(a–b). This carrier redistribution has also been observed in other nonpolar InGaN QW [30]. On the other hand for  $m3$ , no sign of carrier redistribution indicates that photoexcited carriers populate into higher energy states and tend to follow a global Fermi distribution and carrier localization is smaller than in  $m6$ .

Fig. 5 shows the temperature-dependent PL emission spectra of the sample (a–c)  $m6$  and (d–f)  $m3$  in a range of 20–400 °C and under three different excitation power (1, 5 and 50  $\mu\text{W}$ ). The common feature of both samples is the redshifting of peak energy with rising temperature which is attributed to thermal narrowing of bandgap energy. We can also observe strong emission from lower energy centers which is comparable to that from the band-to-band recombination from the extended states. This can possibly be attributed to the localization centers induced from

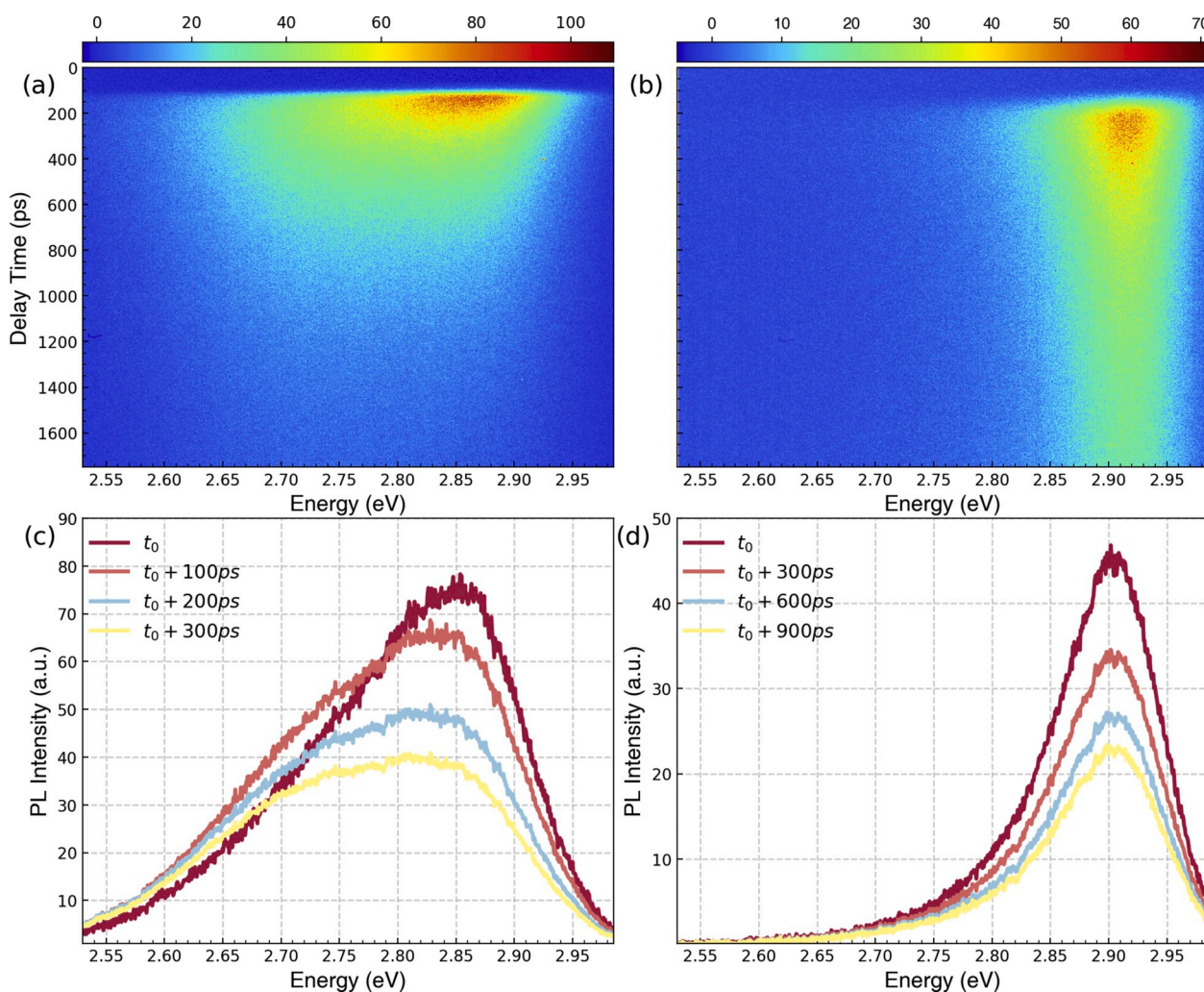


**Fig. 4.** Streak camera spectroscopy images of sample (a) *m6* and (b) *m3* recorded at room temperature. The resonant laser excitation of 400 nm was used. Transient PL spectra after laser excitation of the sample (c) *m6* and (d) *m3*, with an interval of 0.1 ns and 0.3 ns for each curve, are displayed for *m6* and *m3*, respectively.

thickness fluctuation of QW which is also evidenced in Fig. 1 and S1. Previous reports also discovered that this broad emission is related to the surface morphology with pyramidal hillocks in on-axis *m*-plane QW [24, 44]. In addition, the shaded grey areas in each subplot represent the evolution of FWHM values. For *m6*, it first reduces gradually with temperature up to 150 °C and then starts to increase. In contrast, the FWHM of *m3* tends to rise from 50 °C. It's worth noting that the narrowing FWHM of PL indicates the exciton/carrier delocalization with enhanced thermal energy. This also corresponds to the carrier redistribution dynamic observed in *m6* in Fig. 4(c).

To further investigate the underlying physical mechanisms in the temperature-dependent PL emission, we have also extracted both the peak energy and PL FWHM values and fitted them with related models. Fig. 6 present the temperature dependence of PL peak energy for two samples at three different excitation powers which are shown as hollowed circles. The fitted data from the model are displayed with lines. To further elucidate the degree of exciton/carrier localization, we have applied a modified Varshni empirical model [45–47] to fit the data:

$$E_g(T) = E_g(0) - \frac{\alpha T^2}{\beta + T} - \frac{\sigma^2}{k_B T} \quad (6)$$

where  $E_g(0)$  the bandgap energy of InGaN at 0K,  $T$  is temperature in Kelvin,  $k_B$  is the Boltzmann constant,  $\alpha$  and  $\beta$  are the Varshni fitting parameters and  $\sigma$  is a parameter indicative of the degree of exciton localization. A unified Debye temperature  $\beta = 630$  K is used in the fitting

procedure. All  $\sigma$  parameters are also summarized in Fig. 6. We can observe that the degree of exciton localization ( $\sigma$ ) in *m6* is almost twice as large as the ones in *m3*, which is in good agreement with the experimental results from Figs. 3–5. The difference in  $\sigma$  suggests that the exciton localization existed in both samples arise from different physical origins, which is also evidenced in STEM analysis in Fig. 1. In addition compared with the fitted  $\sigma$  values from previous reports,  $\sigma$  values of *m3* are comparable to those from green polar InGaN MQW of  $\sim 30$  meV [48], while *m6* obtains a much higher  $\sigma$ , which also are close to those reported in green semipolar InGaN MQW [46].

To further elucidate exciton-phonon scattering mechanisms at elevated temperatures, we have extracted the full width at half maximum (FWHM) of temperature-dependent PL spectra of both samples and plotted them in Fig. 7(a–c). For *m6*, FWHM first reduces with temperature up to 150 °C ( $\sim 420$ K), which can be attributed to a more homogeneous redistribution of carriers with enhanced thermal energy from surrounding potential minima. Afterwards FWHM tends to rise and the increase is related to both phonon- and impurity-induced broadening mechanisms. In comparison, *m3* exhibits similar rising tendency with temperature above 100 °C except the slight decrease near the room temperature.

Considering that the PL spectrum is convoluted with the emission from both radiative band-to-band recombination and localization sites, we have applied multiple Gaussian functions to fit each spectrum and obtained FWHM from the main peak (extended states) with the strongest

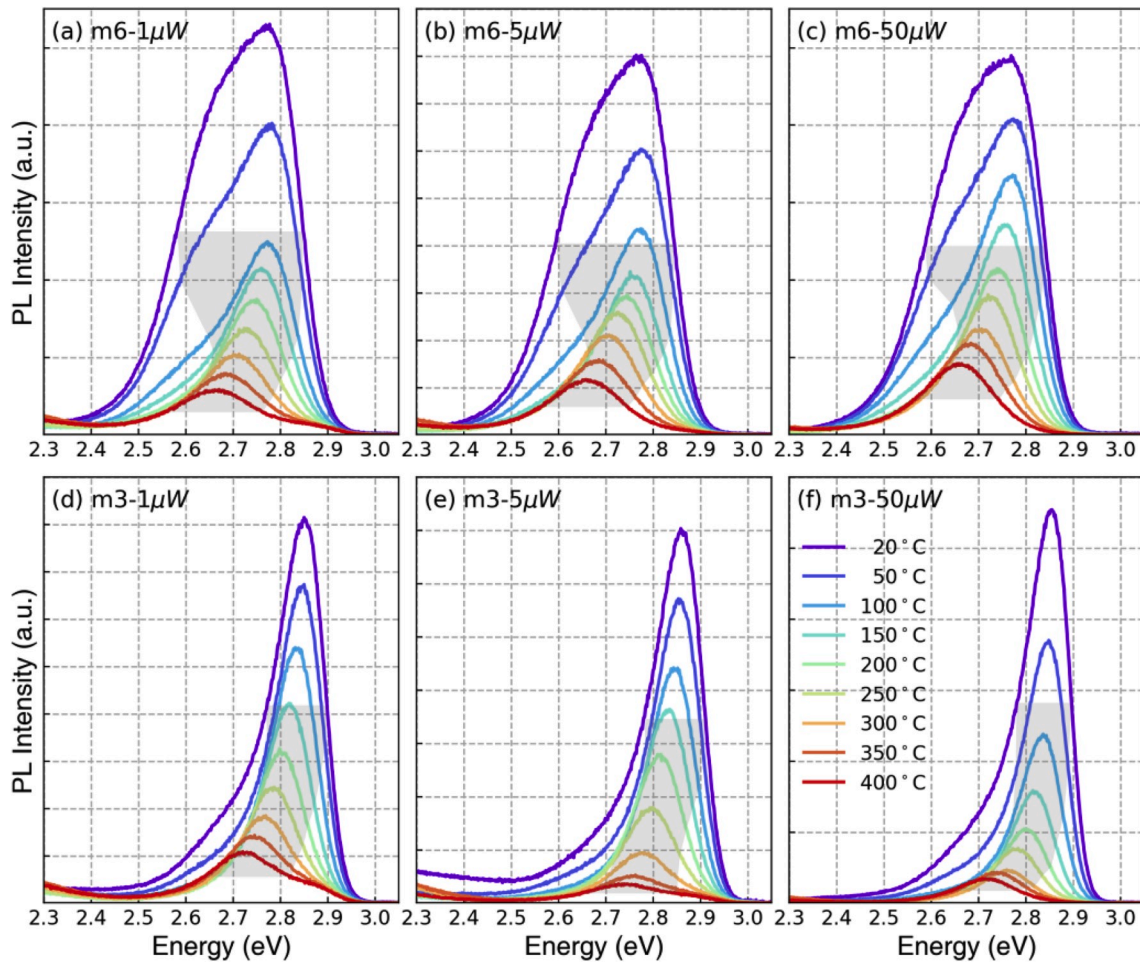


Fig. 5. Temperature-dependent PL emission spectra of the sample (a–c) *m6* and (d–f) *m3* in range of 20–400 °C and under three different excitation power (1, 5 and 50 μW). All data are not normalized. The shaded area indicates the evolution of FWHM of both samples.

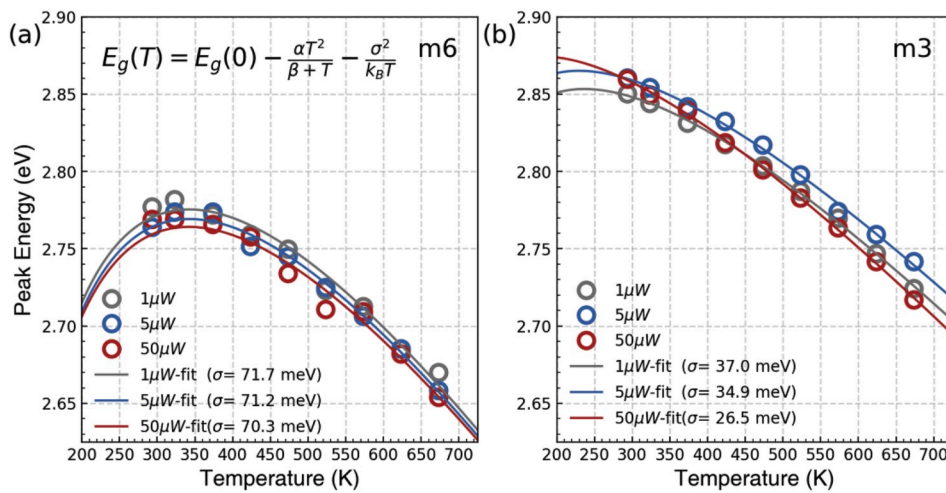
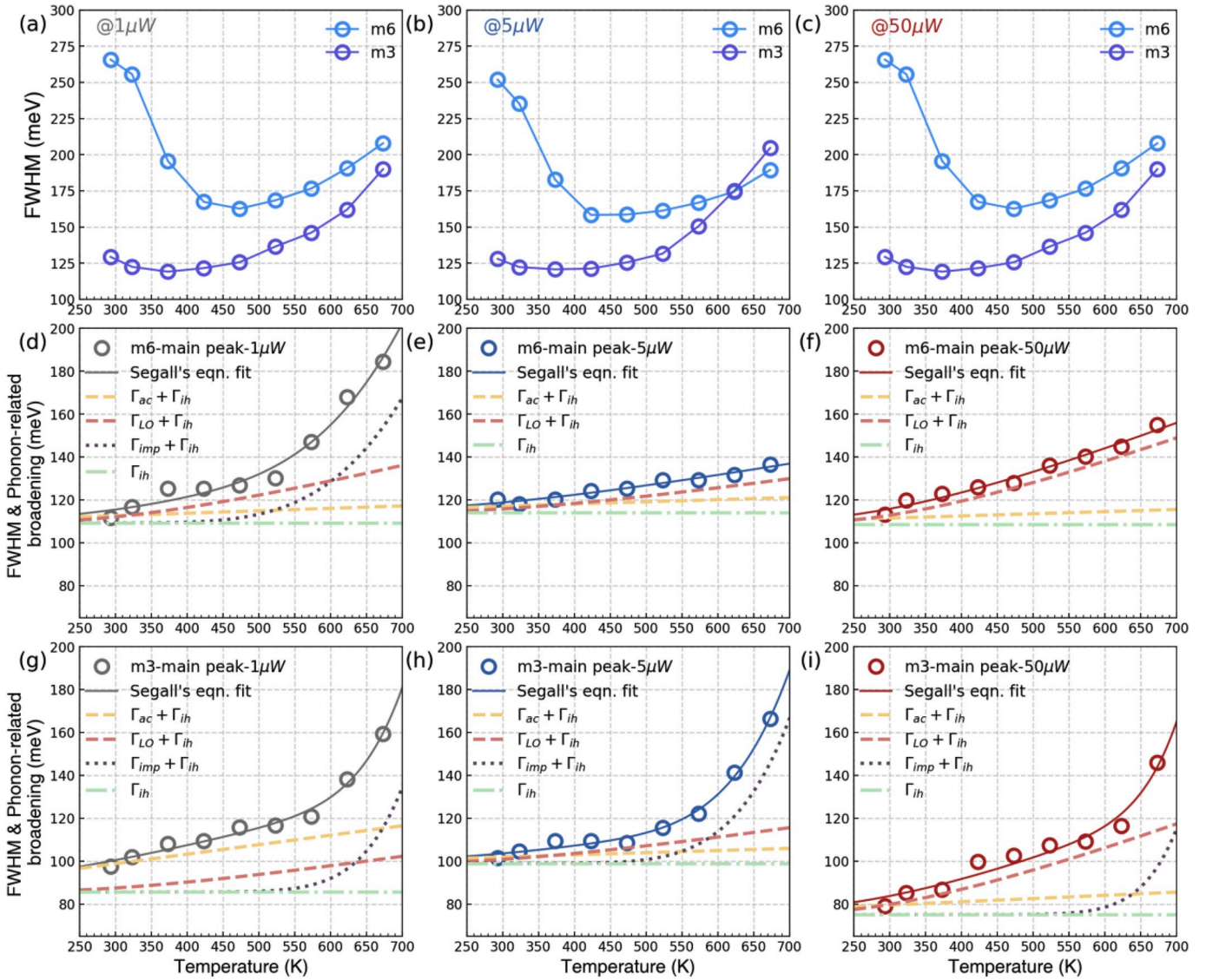


Fig. 6. PL emission peak energy as a function of temperature for sample (a) *m6* and (b) *m3* at three different excitation powers (1 μW for grey, 5 μW for blue and 50 μW for red).

PL emission. The results are shown in Fig. 7(d–f) for *m6* and Fig. 7(g–i) for *m3*, respectively. All extracted FWHM values have been fitted with Segall's equation (see Table 2). The overall broadening of FWHM with temperature can be described as the sum of three types of phonon-induced linewidth broadening mechanisms [49,50] as well as the scattering from ionized impurities [51–53]:

$$\Gamma(T) = \Gamma_{ih} + \Gamma_{ac} + \Gamma_{LO} + \Gamma_{impurity}$$

$$\Gamma(T) = \Gamma_{ih} + \gamma_{ac}T + \frac{\gamma_{LO}}{\exp(E_{LO}/k_B T) - 1} + \gamma_{im} \exp\left(\frac{-E_{imp}}{k_B T}\right), \quad (7)$$



**Fig. 7.** Temperature dependence of PL FWHM of 2 samples. FWHM of the steady-state PL spectra as a function of temperature for (a–c) *m6* (in blue) and *m3* (purple). In Fig. 7(d–i), the hollow circles are the FWHM values of the main peaks in sample *m6* and *m3* by fitting with multiple Gaussian peaks. Grey, blue and red circles correspond to 1  $\mu\text{W}$ , 5  $\mu\text{W}$  and 50  $\mu\text{W}$ . The solid lines in Fig. 7(d–i) are fitted using Segall's expression of  $\Gamma(T) = \Gamma_{ih} + \Gamma_{LO} + \Gamma_{ac} + \Gamma_{impurity}$ , which account for contributions from inhomogeneous broadening, Fröhlich coupling with LO and AC phonons and impurities. The broadening of PL linewidth with temperature arises from inhomogeneous broadening ( $\Gamma_{ih}$ , horizontal green dash-dot line), Fröhlich coupling between charge carriers and LO phonons ( $\Gamma_{LO}$ , red dash line) and acoustic phonons ( $\Gamma_{ac}$ , orange dash line), and scattering from ionized impurities ( $\Gamma_{impurity}$ , brown dotted line).

where  $\Gamma_{ih}$  is the temperature-independent inhomogeneous broadening constant which stems from scattering due to exciton–exciton interactions, crystal disorder and imperfections [49]. In the second and third terms ( $\Gamma_{ac}$  and  $\Gamma_{LO}$ ),  $\gamma_{ac}$  and  $\gamma_{LO}$  are the acoustic and longitudinal optical (LO) phonon coupling constants, respectively [50].  $E_{LO}$  represents the characteristic energy of LO phonon which is set as 91 meV in the fitting procedure. The last term ( $\Gamma_{impurity}$ ) accounts for the scattering from ionized impurities with an average activation energy  $E_{imp}$ . Generally, two major homogeneous broadening mechanisms ( $\Gamma_{ac}$  and  $\Gamma_{LO}$ ) are scattering of deformation potential [54]. The interaction between exciton and acoustic phonon involves only intraband scattering of excitons [50] and is linearly dependent on temperature. In contrast, the interaction between exciton and LO phonon is typically described as Fröhlich interaction, which originates from Coulomb interaction between electrons and electric field induced by the out-of-phase displacements of oppositely charged atoms due to LO phonon. For polar semiconductors such as GaN, LO phonon dominates the scattering

**Table 2**

Parameters determined from fitting for the PL emission from the extended states for *m6* and *m3*.

	$\Gamma_0$ (meV)	$\gamma_{ac}$ ( $\mu\text{eV}/k$ )	$\gamma_{LO}$ (meV)	$E_{LO}$ (meV)	$\gamma_{im}$ (eV)	$E_{imp}$ (eV)
<i>m6</i> – 1 $\mu\text{W}$	109.2	11.4	95.0	91.3 <sup>a</sup>	44.4	0.400
<i>m6</i> – 5 $\mu\text{W}$	114.1	10.0	55.9	91.3 <sup>a</sup>	–	–
<i>m6</i> – 50 $\mu\text{W}$	108.5	10.0	143.2	91.3 <sup>a</sup>	–	–
<i>m3</i> – 1 $\mu\text{W}$	90.6	24.4	90.0	91.3 <sup>a</sup>	10000	0.739
<i>m3</i> – 5 $\mu\text{W}$	98.9	10.0	55.0	91.3 <sup>a</sup>	599.5	0.548
<i>m3</i> – 50 $\mu\text{W}$	75.0	15.0	139.8	91.3 <sup>a</sup>	10000	0.888

<sup>a</sup> The numbers with asterisks (\*) mean that they are fixed in the fitting.

mechanism [45,49].

For  $m_6$ , the contribution of impurity broadening ( $\Gamma_{\text{impurity}}$ ) can only be observed under 1  $\mu\text{W}$  excitation. Acoustic phonon broadening ( $\Gamma_{\text{ac}}$ ) dominates under 5  $\mu\text{W}$  while LO phonon broadening is the main broadening mechanism under 50  $\mu\text{W}$ . From Fig. 7(g) to 7(i), the broadening of FWHM of  $m_3$  is dominated mostly by both acoustic and LO phonon scattering prior to 600K. Under low excitation conditions including 1  $\mu\text{W}$  and 5  $\mu\text{W}$ , the crossover temperature where these two homogeneous broadening mechanisms contribute equally is approximately 400K. After 600K, impurity scattering ( $\Gamma_{\text{impurity}}$ ) becomes dominant. Previous paper suggested that this activation energy could also provide an estimated localization depth of excited carriers dephasing into surrounding InGaN materials [52,55]. However, an even wider temperature range of measurements and further investigation are necessary to reach a conclusive argument on this topic.

### 3. Conclusions

In conclusion, experimental investigations on two  $m$ -plane InGaN/GaN QWs demonstrate that in relatively thin QW structure, the obscure interfaces between QW and barriers and the lack of structural uniformity induced from Indium compositional fluctuation tend to delocalize carriers and make them more prone to the nonradiative Shockley-Reed-Hall recombination. Nonetheless in the case of thick QW design, carrier localization is more likely to originate from thickness fluctuation of QW and/or barrier which enables InGaN QWs maintain strong radiative capability even at elevated temperatures. It's therefore vital for device designers to carefully manage QW integrity and uniformity in pursuit of a thicker  $m$ -plane InGaN active region. From the analysis of temperature-dependent carrier lifetime, the major carrier delocalization mechanism at elevated temperatures is possibly thermal escape of electron from QW. In addition, detailed analysis on exciton-phonon scattering mechanisms reveals that both acoustic and optical phonon scatterings play the dominant roles in the range of 300–600 K and afterwards impurity scattering is the main mechanism responsible for FWHM broadening. These results offer new insights and strategies for further development of InGaN-based optoelectronics toward the theoretical limit of their efficiency.

### 4. Methods

#### 4.1. Growth and structure parameters of nonpolar InGaN/GaN MQWs

Two InGaN/GaN MQW on nonpolar  $m$ -plane substrates were grown by conventional metal-organic chemical vapor deposition (MOCVD). The freestanding nominally on-axis bulk  $m$ -plane GaN substrates with low defect density ( $\sim 10^6 \text{ cm}^{-2}$ ) were provided from commercial vendors. The growth condition was designed to achieve the indium incorporation around 12–14% in samples. The designed device consists of 1  $\mu\text{m}$  Si-doped n-GaN ( $[\text{Si}] = 5 \times 10^{18} \text{ cm}^{-3}$ ), 10 nm highly Si-doped  $n^+$ -GaN ( $[\text{Si}] = 1 \times 10^{19} \text{ cm}^{-3}$ ), 20 periods of InGaN (nominal 3 or 6 nm)/GaN (10 nm) MQWs, 30 nm Mg-doped smooth  $p^+$ -GaN ( $[\text{Mg}] = 1 \times 10^{19} \text{ cm}^{-3}$ ), 120 nm Mg-doped p-GaN ( $[\text{Mg}] = 3 \times 10^{19} \text{ cm}^{-3}$ ), and 10 nm highly Mg-doped  $p^+$ -GaN contact layer ( $[\text{Mg}] = 1 \times 10^{20} \text{ cm}^{-3}$ ).

#### 4.2. FIB and STEM imaging

The nonpolar InGaN/GaN specimens for STEM imaging were prepared with a FEI Nova 200 Dual-Beam FIB system with a Ga ion source. A JEOL-ARM200F scanning transmission electron microscopy (STEM) operated at 200 KV and equipped with double aberration-correctors for both probe-forming and imaging lenses was used to perform high-angle annular-dark field (HAADF) imaging.

#### 4.3. Temperature-dependent photoluminescence and time-resolved photoluminescence measurements

PL and TRPL measurements were done using a home-built system, where a picosecond 405nm pulsed laser diode (PDL 800-B) was used as excitation source. PL spectrum was collected by a Si array detector coupled with Horiba monochromator (TRIAX 320). TRPL was measured by a time-correlated single-photon counting system (TCSPC). A Si photomultiplier tube (PMT) detector is attached at the other output port of monochromator and its signal is then recorded by TCSPC board (SPC130 module).

A Linkam HFS600-PB4 stage capable of heating the samples up to 600  $^\circ\text{C}$  was used to perform the temperature-dependent measurements. For both PL and TRPL measurements, the temperature of the stage was increased from room temperature to 400  $^\circ\text{C}$  in steps of 25–50  $^\circ\text{C}$  with a ramp rate of 10–20  $^\circ\text{C}/\text{min}$ . Once the desired temperature was reached, the sample was kept at the specified temperature for another 5 min.

#### 4.4. Streak camera spectroscopy measurement

The Picosecond–microsecond time-resolved fluorescence Spectrometer, Streak Camera System consists of a femtosecond Titanium:Sapphire laser system operated at both MHz and KHz repetition rates (Coherent). The MHz system is a broadband Ti:S oscillator coupled with a pulse selector and a second harmonic generator, covers a wavelength region from 700 – 1000 nm and 350–500 nm and a repetition rate from single shot (1 Hz) to 76 MHz. The KHz system uses the MHz oscillator as a seed laser to pump a regenerative amplifier and an OPA operated between 100 – 250 KHz. The output wavelength covers from 250 – 750 nm. The detecting system consists of a spectrograph, a streak camera with fast and a slow time sweep unit. The system is designed to record fluorescence signal as a function of time and wavelength with a time resolution of 5 ps and wavelength region from 320 – 950 nm.

#### 4.5. Simulation of band diagrams

The energy band diagrams of InGaN/GaN double heterostructures were simulated using Silvaco ATLAS software. They contain 3- or 6-nm absorbing layer and 10-nm barrier. The band structure parameters, the conduction and valence band offsets of InGaN/GaN DHs were obtained from Huang et al. [17], respectively. Silvaco ATLAS is a commercial device simulation tool based on the drift-diffusion model. MQW simulation is based on a parabolic quantum well model implemented within Silvaco ATLAS. The bound state energies are calculated solving the Schrödinger equation along discrete slices in the quantization direction.

#### Declaration of competing interest

The authors declare that they have no known competing financial interests or personal relationships that could have appeared to influence the work reported in this paper.

#### CRediT authorship contribution statement

**Xuanqi Huang:** Conceptualization, Methodology, Investigation, Validation, Data curation, Formal analysis, Visualization, Supervision, Writing - original draft, Writing - review & editing. **Dongying Li:** Formal analysis, Investigation, Resources, Writing - review & editing. **Po-Yi Su:** Formal analysis, Investigation, Resources, Writing - review & editing. **Houqiang Fu:** Formal analysis, Investigation. **Hong Chen:** Formal analysis, Investigation. **Chen Yang:** Investigation. **Jingan Zhou:** Investigation. **Xin Qi:** Investigation. **Tsung-Han Yang:** Investigation. **Jossue Montes:** Investigation. **Xuguang Deng:** Investigation. **Kai Fu:** Investigation. **Steven P. DenBaars:** Investigation, Resources. **Shuji Nakamura:** Investigation, Resources. **Fernando A. Ponce:** Formal analysis, Investigation, Resources, Writing - review & editing. **Cun-**

**Zheng Ning:** Formal analysis, Investigation, Resources, Writing - review & editing. **Yuji Zhao:** Formal analysis, Supervision, Writing - original draft, Writing - review & editing, Funding acquisition.

## Acknowledgements

This work was supported by an NSF award (Award. No. 1809796). S. P. DenBaars and S. Nakamura acknowledge the support of the Solid State Lighting and Energy Electronics Center (SSLEEC) at University of California Santa Barbara (UCSB). We gratefully acknowledge the use of facilities within the LeRoy Eyring Center for Solid State Science, CLAS Ultra-Fast Laser Facility and the ASU Nanofab at Arizona State University. This work was supported, in part, by NSF award number NNCI – 1542160.

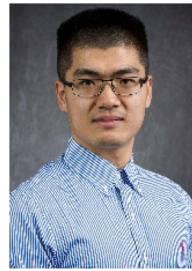
## Appendix A. Supplementary data

Supplementary data to this article can be found online at <https://doi.org/10.1016/j.nanoen.2020.105013>.

## References

- [1] Y. Zhao, H. Fu, G.T. Wang, S. Nakamura, Toward ultimate efficiency: progress and prospects on planar and 3D nanostructured nonpolar and semipolar InGaN light-emitting diodes, *Adv. Optic Photon* 10 (2018) 246, <https://doi.org/10.1364/AOP.10.000246>.
- [2] C. Weisbuch, M. Piccaro, L. Martinelli, J. Iveland, J. Peretti, J.S. Speck, The efficiency challenge of nitride light-emitting diodes for lighting, *Phys. Status Solidi* 212 (2015) 899–913, <https://doi.org/10.1002/pssa.201431868>.
- [3] H. Fu, Z. Lu, X. Huang, H. Chen, Y. Zhao, Crystal orientation dependent intersubband transition in semipolar AlGaIn/GaN single quantum well for optoelectronic applications, *J. Appl. Phys.* 119 (2016) 174502, <https://doi.org/10.1063/1.4948667>.
- [4] M. Kneissl, T.-Y. Seong, J. Han, H. Amano, The emergence and prospects of deep-ultraviolet light-emitting diode technologies, *Nat. Photon.* 13 (2019) 233–244, <https://doi.org/10.1038/s41566-019-0359-9>.
- [5] F.A. Chowdhury, M.L. Trudeau, H. Guo, Z. Mi, A photochemical diode artificial photosynthesis system for unassisted high efficiency overall pure water splitting, *Nat. Commun.* 9 (2018) 1707, <https://doi.org/10.1038/s41467-018-04067-1>.
- [6] S. Wang, H. Long, Y. Zhang, Q. Chen, J. Dai, S. Zhang, J. Chen, R. Liang, L. Xu, F. Wu, Z.-H. Zhang, H. Sun, C. Chen, Y. Gao, Monolithic integration of deep ultraviolet LED with a multiplicative photoelectric converter, *Nano Energy* 66 (2019) 104181, <https://doi.org/10.1016/j.nanoen.2019.104181>.
- [7] C.-Y. Huang, T.-Y. Tai, J.-J. Lin, T.-C. Chang, C.-Y. Liu, T.-C. Lu, Y.-R. Wu, H.-C. Kuo, Mode-hopping phenomena in the InGaN-based core-shell nanorod array collective lasing, *ACS Photonics* 5 (2018) 2724–2729, <https://doi.org/10.1021/acsp.8b00471>.
- [8] R. Lin, V. Mazzone, N. Alfaraj, J. Liu, X. Li, A. Fratallocchi, On-chip hyperuniform lasers for controllable transitions in disordered systems, *Laser Photon. Rev.* 14 (2020) 1800296, <https://doi.org/10.1002/lpor.201800296>.
- [9] H. Amano, Y. Baines, E. Beam, M. Borgia, T. Bouchet, P.R. Chalker, M. Charles, K. J. Chen, N. Chowdhury, R. Chu, C. De Santi, M.M. De Souza, S. Decoutere, L. Di Cioccio, B. Eckardt, T. Egawa, P. Fay, J.J. Freedman, L. Guido, O. Häberlein, G. Haynes, T. Heckel, D. Hemakumara, P. Houston, J. Hu, M. Hua, Q. Huang, A. Huang, S. Jiang, H. Kawai, D. Kinzer, M. Kuball, A. Kumar, K.B. Lee, X. Li, D. Marcon, M. März, R. McCarthy, G. Meneghesso, M. Meneghini, E. Morvan, A. Nakajima, E.M.S. Narayanan, S. Oliver, T. Palacios, D. Piedra, M. Plissonnier, R. Reddy, M. Sun, I. Thayne, A. Torres, N. Trivellin, V. Unni, M.J. Uren, M. Van Hove, D.J. Wallis, J. Wang, J. Xie, S. Yagi, S. Yang, C. Youtsey, R. Yu, E. Zanoni, S. Zeltner, Y. Zhang, The 2018 GaN power electronics roadmap, *J. Phys. Appl. Phys.* 51 (2018) 163001, <https://doi.org/10.1088/1361-6463/aaaf9d>.
- [10] H. Fu, K. Fu, X. Huang, H. Chen, I. Baranowski, T.H. Yang, J. Montes, Y. Zhao, High performance vertical GaN-on-GaN p-n power diodes with hydrogen-plasma-based edge termination, *IEEE Electron. Device Lett.* 39 (2018) 1018–1021, <https://doi.org/10.1109/LED.2018.2837625>.
- [11] T. Kachi, Recent progress of GaN power devices for automotive applications, *Jpn. J. Appl. Phys.* 53 (2014) 100210, <https://doi.org/10.7567/JJAP.53.100210>.
- [12] X. Huang, R. Fang, C. Yang, K. Fu, H. Fu, H. Chen, T.-H. Yang, J. Zhou, J. Montes, M. Kozicki, H. Barnaby, B. Zhang, Y. Zhao, Steep-slope field-effect transistors with AlGaIn/GaN HEMT and oxide-based threshold switching device, *Nanotechnology* 30 (2019) 215201, <https://doi.org/10.1088/1361-6528/ab0484>.
- [13] A. Chakraborty, B.A. Haskell, S. Keller, J.S. Speck, S.P. DenBaars, S. Nakamura, U. K. Mishra, Demonstration of nonpolar m-plane InGaN/GaN light-emitting diodes on free-standing m-plane GaN substrates, *Jpn. J. Appl. Phys.* 44 (2005) L173, <https://doi.org/10.1143/JJAP.44.L173>.
- [14] K.-C. Kim, M.C. Schmidt, H. Sato, F. Wu, N. Fellows, M. Saito, K. Fujito, J.S. Speck, S. Nakamura, S.P. DenBaars, Improved electroluminescence on nonpolar m-plane InGaN/GaN quantum wells LEDs, *Phys. Status Solidi RRL – Rapid Res. Lett.* 1 (2007) 125–127, <https://doi.org/10.1002/pssr.200701061>.
- [15] K. Okamoto, H. Ohta, S.F. Chichibu, J. Ichihara, H. Takasu, Continuous-wave operation of m-plane InGaN multiple quantum well laser diodes, *Jpn. J. Appl. Phys.* 46 (2007) L187, <https://doi.org/10.1143/JJAP.46.L187>.
- [16] M.C. Schmidt, K.-C. Kim, R.M. Farrell, D.F. Feezell, D.A. Cohen, M. Saito, K. Fujito, J.S. Speck, S.P. DenBaars, S. Nakamura, Demonstration of nonpolar m-plane InGaN/GaN laser diodes, *Jpn. J. Appl. Phys.* 46 (2007) L190, <https://doi.org/10.1143/JJAP.46.L190>.
- [17] X. Huang, H. Fu, H. Chen, X. Zhang, Z. Lu, J. Montes, M. Iza, S.P. DenBaars, S. Nakamura, Y. Zhao, Nonpolar and semipolar InGaN/GaN multiple-quantum-well solar cells with improved carrier collection efficiency, *Appl. Phys. Lett.* 110 (2017) 161105, <https://doi.org/10.1063/1.4980139>.
- [18] X. Huang, W. Li, H. Fu, D. Li, C. Zhang, H. Chen, Y. Fang, K. Fu, S.P. DenBaars, S. Nakamura, S.M. Goodnick, C.-Z. Ning, S. Fan, Y. Zhao, High-temperature polarization-free III-nitride solar cells with self-cooling effects, *ACS Photonics* 6 (2019) 2096–2103, <https://doi.org/10.1021/acsp.9b00655>.
- [19] H. Fu, X. Zhang, K. Fu, H. Liu, S.R. Alugubelli, X. Huang, H. Chen, I. Baranowski, T.-H. Yang, K. Xu, F.A. Ponce, B. Zhang, Y. Zhao, Nonpolar vertical GaN-on-GaN p-n diodes grown on free-standing  $\sqrt{10}$  m-plane GaN substrates, *APEX* 11 (2018) 111003, <https://doi.org/10.7567/APEX.11.111003>.
- [20] M. Monavarian, G. Pickrell, A.A. Aragon, I. Stricklin, M.H. Crawford, A. A. Allerman, K.C. Celio, F. Léonard, A.A. Talin, A.M. Armstrong, D. Feezell, High-voltage regrown nonpolar m-plane vertical p-n diodes: a step toward future selective-area-doped power switches, *IEEE Electron. Device Lett.* 40 (2019) 387–390, <https://doi.org/10.1109/LED.2019.2892345>.
- [21] Y. Zhao, Q. Yan, C.-Y. Huang, S.-C. Huang, P.S. Hsu, S. Tanaka, C.-C. Pan, Y. Kawaguchi, K. Fujito, C.G.V. de Walle, J.S. Speck, S.P. DenBaars, S. Nakamura, D. Feezell, Indium incorporation and emission properties of nonpolar and semipolar InGaN quantum wells, *Appl. Phys. Lett.* 100 (2012) 201108, <https://doi.org/10.1063/1.4719100>.
- [22] S. Nakagawa, H. Tsujimura, K. Okamoto, M. Kubota, H. Ohta, Temperature dependence of polarized electroluminescence from nonpolar m-plane InGaN-based light emitting diodes, *Appl. Phys. Lett.* 91 (2007) 171110, <https://doi.org/10.1063/1.2800817>.
- [23] T.J. Badcock, M. Ali, T. Zhu, M. Pristovsek, R.A. Oliver, A.J. Shields, Radiative recombination mechanisms in polar and non-polar InGaN/GaN quantum well LED structures, *Appl. Phys. Lett.* 109 (2016) 151110, <https://doi.org/10.1063/1.4964842>.
- [24] K.M. Kelchner, L.Y. Kuritzky, K. Fujito, S. Nakamura, S.P. DenBaars, J.S. Speck, Emission characteristics of single InGaN quantum wells on misoriented nonpolar m-plane bulk GaN substrates, *J. Cryst. Growth* 382 (2013) 80–86, <https://doi.org/10.1016/j.jcrysgro.2013.08.013>.
- [25] W. Liu, R. Butté, A. Dussaigne, N. Grandjean, B. Deveaud, G. Jacopin, Carrier-density-dependent recombination dynamics of excitons and electron-hole plasma in m-plane InGaN/GaN quantum wells, *Phys. Rev. B* 94 (2016), <https://doi.org/10.1103/PhysRevB.94.195411>.
- [26] T.J. Badcock, R. Hao, M.A. Moram, M.J. Kappers, P. Dawson, R.A. Oliver, C. J. Humphreys, Recombination mechanisms in heteroepitaxial non-polar InGaN/GaN quantum wells, *J. Appl. Phys.* 112 (2012), 013534, <https://doi.org/10.1063/1.4731730>.
- [27] P. Dawson, S. Schulz, R.A. Oliver, M.J. Kappers, C.J. Humphreys, The nature of carrier localisation in polar and nonpolar InGaN/GaN quantum wells, *J. Appl. Phys.* 119 (2016) 181505, <https://doi.org/10.1063/1.4948237>.
- [28] S. Schulz, D.P. Tanner, E.P. O'Reilly, M.A. Caro, T.L. Martin, P.A.J. Bagot, M. P. Moody, F. Tang, J.T. Griffiths, F. Oehler, M.J. Kappers, R.A. Oliver, C. J. Humphreys, D. Sutherland, M.J. Davies, P. Dawson, Structural, electronic, and optical properties of m-plane InGaN/GaN quantum wells: insights from experiment and atomistic theory, *Phys. Rev. B* 92 (2015) 235419, <https://doi.org/10.1103/PhysRevB.92.235419>.
- [29] C. Mounir, U.T. Schwarz, I.L. Koslow, M. Kneissl, T. Wernicke, T. Schimpke, M. Strassburg, Impact of inhomogeneous broadening on optical polarization of high-inclination semipolar and nonpolar  $\sqrt{10}$  m-plane InGaN quantum wells, *Phys. Rev. B* 93 (2016) 235314, <https://doi.org/10.1103/PhysRevB.93.235314>.
- [30] S. Marcinkevicius, K.M. Kelchner, S. Nakamura, S.P. DenBaars, J.S. Speck, Optical properties and carrier dynamics in m-plane InGaN quantum wells, *Phys. Status Solidi C* 11 (2014) 690–693, <https://doi.org/10.1002/pssc.201300430>.
- [31] C. Netzal, C. Mauder, T. Wernicke, B. Reuters, H. Kalisch, M. Heuken, A. Vescan, M. Weyers, M. Kneissl, Strong charge carrier localization interacting with extensive nonradiative recombination in heteroepitaxially grown m-plane GaInN quantum wells, *Semicond. Sci. Technol.* 26 (2011) 105017, <https://doi.org/10.1088/0268-1242/26/10/105017>.
- [32] S. Marcinkevicius, K.M. Kelchner, L.Y. Kuritzky, S. Nakamura, S.P. DenBaars, J. S. Speck, Photoexcited carrier recombination in wide m-plane InGaN/GaN quantum wells, *Appl. Phys. Lett.* 103 (2013) 111107, <https://doi.org/10.1063/1.4820839>.
- [33] M. Shahmohammadi, W. Liu, G. Rossbach, L. Lahourcade, A. Dussaigne, C. Bougerol, R. Butté, N. Grandjean, B. Deveaud, G. Jacopin, Enhancement of Auger recombination induced by carrier localization in InGaN/GaN quantum wells, *Phys. Rev. B* 95 (2017) 125314, <https://doi.org/10.1103/PhysRevB.95.125314>.
- [34] Q.L. Zhang, F.Y. Meng, P.A. Crozier, N. Newman, S. Mahajan, Effects of stress on phase separation in InGa<sub>1-x</sub>N/GaN multiple quantum-wells, *Acta Mater.* 59 (2011) 3759–3769, <https://doi.org/10.1016/j.actamat.2010.11.020>.
- [35] S. Pereira, M.R. Correia, E. Pereira, K.P. O'Donnell, C. Trager-Cowan, F. Sweeney, E. Alves, Compositional pulling effects in  $\sqrt{10}$  m-plane InGaN/GaN quantum wells, *Appl. Phys. Lett.* 103 (2013) 111107, <https://doi.org/10.1063/1.4820839>.

- combined depth-resolved cathodoluminescence and Rutherford backscattering/channeling study, *Phys. Rev. B* 64 (2001) 205311, <https://doi.org/10.1103/PhysRevB.64.205311>.
- [36] Y. Lee, C. Chiu, C.C. Ke, P.C. Lin, T. Lu, H. Kuo, S. Wang, Study of the excitation power dependent internal quantum efficiency in InGaN/GaN LEDs grown on patterned sapphire substrate, *IEEE J. Sel. Top. Quant. Electron.* 15 (2009) 1137–1143, <https://doi.org/10.1109/JSTQE.2009.2014967>.
- [37] H. Wang, Z. Ji, S. Qu, G. Wang, Y. Jiang, B. Liu, X. Xu, H. Mino, Influence of excitation power and temperature on photoluminescence in InGaN/GaN multiple quantum wells, *Optic Express* 20 (2012) 3932–3940, <https://doi.org/10.1364/OE.20.003932>.
- [38] P. Corfdir, J. Levrat, A. Dussaigne, P. Lefebvre, H. Teisseyre, I. Grzegory, T. Suski, J.-D. Ganière, N. Grandjean, B. Deveaud-Plédran, Intrinsic dynamics of weakly and strongly confined excitons in nonpolar nitride-based heterostructures, *Phys. Rev. B* 83 (2011) 245326, <https://doi.org/10.1103/PhysRevB.83.245326>.
- [39] J. Bellessa, V. Voliotis, R. Grousson, X.L. Wang, M. Ogura, H. Matsuhata, Quantum-size effects on radiative lifetimes and relaxation of excitons in semiconductor nanostructures, *Phys. Rev. B* 58 (1998) 9933–9940, <https://doi.org/10.1103/PhysRevB.58.9933>.
- [40] L.C. Andreani, F. Tassone, F. Bassani, Radiative lifetime of free excitons in quantum wells, *Solid State Commun.* 77 (1991) 641–645, [https://doi.org/10.1016/0038-1098\(91\)90761-J](https://doi.org/10.1016/0038-1098(91)90761-J).
- [41] B. Deveaud, T.C. Damen, J. Shah, C.W. Tu, Dynamics of exciton transfer between monolayer-flat islands in single quantum wells, *Appl. Phys. Lett.* 51 (1987) 828–830, <https://doi.org/10.1063/1.98826>.
- [42] Y.-R. Wu, R. Shivaraman, K.-C. Wang, J.S. Speck, Analyzing the physical properties of InGaN multiple quantum well light emitting diodes from nano scale structure, *Appl. Phys. Lett.* 101 (2012), 083505, <https://doi.org/10.1063/1.4747532>.
- [43] S. Khatsevich, D.H. Rich, The effects of crystallographic orientation and strain on the properties of excitonic emission from wurtzite InGaN/GaN quantum wells, *J. Phys. Condens. Matter* 20 (2008) 215223, <https://doi.org/10.1088/0953-8984/20/21/215223>.
- [44] T. Zhu, D. Gachet, F. Tang, W.Y. Fu, F. Oehler, M.J. Kappers, P. Dawson, C. J. Humphreys, R.A. Oliver, Local carrier recombination and associated dynamics in *m*-plane InGaN/GaN quantum wells probed by picosecond cathodoluminescence, *Appl. Phys. Lett.* 109 (2016) 232103, <https://doi.org/10.1063/1.4971366>.
- [45] W. Bao, Z. Su, C. Zheng, J. Ning, S. Xu, Carrier localization effects in InGaN/GaN multiple-quantum-wells LED nanowires: luminescence quantum efficiency improvement and “negative” thermal activation energy, *Sci. Rep.* 6 (2016) 34545, <https://doi.org/10.1038/srep34545>.
- [46] D.V. Dinh, S. Presa, P.P. Maaskant, B. Corbett, P.J. Parbrook, Exciton localization in polar and semipolar (112<sup>-</sup>) In<sub>0.2</sub>Ga<sub>0.8</sub>N/GaN multiple quantum wells, *Semicond. Sci. Technol.* 31 (2016), 085006, <https://doi.org/10.1088/0268-1242/31/8/085006>.
- [47] T. Lu, Z. Ma, C. Du, Y. Fang, H. Wu, Y. Jiang, L. Wang, L. Dai, H. Jia, W. Liu, H. Chen, Temperature-dependent photoluminescence in light-emitting diodes, *Sci. Rep.* 4 (2015) 6131, <https://doi.org/10.1038/srep06131>.
- [48] X.H. Zheng, H. Chen, Z.B. Yan, D.S. Li, H.B. Yu, Q. Huang, J.M. Zhou, Influence of the deposition time of barrier layers on optical and structural properties of high-efficiency green-light-emitting InGaN/GaN multiple quantum wells, *J. Appl. Phys.* 96 (2004) 1899–1903, <https://doi.org/10.1063/1.1769099>.
- [49] S. Rudin, T.L. Reinecke, B. Segall, Temperature-dependent exciton linewidths in semiconductors, *Phys. Rev. B* 42 (1990) 11218–11231, <https://doi.org/10.1103/PhysRevB.42.11218>.
- [50] A.K. Viswanath, J.I. Lee, D. Kim, C.R. Lee, J.Y. Leem, Exciton-phonon interactions, exciton binding energy, and their importance in the realization of room-temperature semiconductor lasers based on GaN, *Phys. Rev. B* 58 (1998) 16333–16339, <https://doi.org/10.1103/PhysRevB.58.16333>.
- [51] J. Lee, E.S. Koteles, M.O. Vassell, Luminescence linewidths of excitons in GaAs quantum wells below 150 K, *Phys. Rev. B* 33 (1986) 5512–5516, <https://doi.org/10.1103/PhysRevB.33.5512>.
- [52] R. Seguin, S. Rodt, A. Strittmatter, L. Reißmann, T. Bartel, A. Hoffmann, D. Bimberg, E. Hahn, D. Gerthsen, Multi-excitonic complexes in single InGaN quantum dots, *Appl. Phys. Lett.* 84 (2004) 4023–4025, <https://doi.org/10.1063/1.1751214>.
- [53] R. Saran, A. Heuer-Jungemann, A.G. Kanaras, R.J. Curry, Giant bandgap renormalization and exciton-phonon scattering in perovskite nanocrystals, *Adv. Opt. Mater.* 5 (2017) 1700231, <https://doi.org/10.1002/adom.201700231>.
- [54] A.D. Wright, C. Verdi, R.L. Milot, G.E. Eperon, M.A. Pérez-Osorio, H.J. Snaith, F. Giustino, M.B. Johnston, L.M. Herz, Electron-phonon coupling in hybrid lead halide perovskites, *Nat. Commun.* 7 (2016) 1–9, <https://doi.org/10.1038/ncomms11755>.
- [55] A. Caria, C.D. Santi, F. Zamperetti, X. Huang, H. Fu, H. Chen, Y. Zhao, G. Meneghesso, E. Zanoni, M. Meneghini, Degradation and recovery of high-periodicity InGaN/GaN MQWs under optical stress in short-circuit condition, in: *Gallium Nitride Mater. Devices XV*, International Society for Optics and Photonics, 2020, p. 112800E, <https://doi.org/10.1117/12.2547590>.



**Xuanqi Huang** received the Ph.D. degree in electrical engineering from the School of Electrical, Computer, and Energy Engineering, Arizona State University, USA in 2020, and the B.S degree in Material Physics from Fudan University, China in 2015. His research interests include III-nitride power electronics, optoelectronics, and optical devices.



**Dongying Li** received her B.S. degree in Applied Physics from Northwestern Polytechnical University in 2016. She is currently pursuing a Ph.D. in Electrical Engineering at Arizona State University under supervision of Professor Cun-Zheng Ning. Her research focuses on optical spectroscopy study of black phosphorus and emitting devices based on 2D materials.



**Po-Yi Su** received his B.S. degree in Materials Science and Engineering from National Cheng Kung University in 2014. He is currently pursuing his Ph.D. in Materials Science and Engineering at Arizona State University under supervision of Professor Fernando Ponce. His research focuses on characterization of the structural and optical properties of III-V semiconductor materials for photovoltaics and power electronic applications.



**Houqiang Fu** received the Ph.D. degree (Highest Hons.) in electrical engineering from the School of Electrical, Computer, and Energy Engineering, Arizona State University (Palais Outstanding Doctoral Student Award). He joined Iowa State University as an Assistant Professor in 2020, before which he was a Postdoctoral Research at Arizona State University. His research expertise and interests include III-nitride power electronics and photonics, wide bandgap semiconductors, semiconductor devices and physics, MOCVD/MBE epitaxial growth, extreme-environment devices and systems, and RF/microwave devices and ICs.



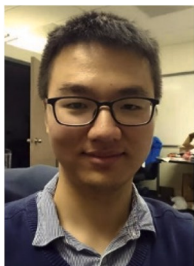
**Hong Chen** received the B.S degree in optical science from Huazhong University of Science and Technology (HUST), Wuhan, China, in 2015. He is currently pursuing the Ph.D. degree in electrical engineering from Arizona State University, Tempe, USA. His research interests include III-nitride based optoelectronic devices and integrated photonics.



**Chen Yang** is currently pursuing the Ph.D. degree with the School of Electrical, Computer, and Energy Engineering, Arizona State University, USA, and received his M.S. degree in Material Physics & Chemistry in 2018 and B.S. degree in Material Physics in 2015 from Fudan University, China. His research interests include III-nitride power electronics, optoelectronics, optical devices, and visible light communication.



**Xuguang Deng** is an engineer with Suzhou Institute of Nano-Tech and Nano-Bionics (SINANO), CAS and currently a visiting scholar with the School of Electrical, Computer, and Energy Engineering, Arizona State University, USA. His research interests are in the fields of III-nitride power electronics, optoelectronics, optical devices, and visible light communication.



**Jingan Zhou** is currently pursuing the Ph.D. degree with the School of Electrical, Computer, and Energy Engineering, Arizona State University, USA. His research interests include III-nitride power electronics, optoelectronics, optical devices, and visible light communication.



**Kai Fu** received the B.S. degree in physics from the Ocean University of China, Qingdao, in 2008 and the Ph.D. degree in microelectronics and solid state electronics from Suzhou Institute of Nano-Tech and Nano-Bionics (SINANO), Chinese Academy of Sciences (CAS), China, Suzhou, in 2013. He is currently an Assistant Research Scientist with the School of Electrical, Computer and Energy Engineering, Arizona State University, Tempe, USA. His research interests include III-nitride power electronics and optoelectronics, and other wide bandgap semiconductors.



**Xin Qi** received the B.S. degree in astronomy and the M.S. degree in optics from Peking University, China, in 2016 and 2019, respectively. He is currently pursuing the Ph.D. degree with the School of Electrical, Computer, and Energy Engineering, Arizona State University, USA. His research interests include power electronics, optoelectronics and optical devices based on III-nitride semiconductors.



**Steven P. DenBaars** is a Mitsubishi Distinguished Professor at the University of California Santa Barbara and the Executive Director of the Solid State Lighting and Energy Electronics Center. He is a recipient of the NSF Presidential Young Investigator Award in 1994, the ICS Young Scientist Award in 1998, the IEEE Fellow Award in 2007, and the IEEE Aron Kressel Award in 2010. He is a fellow of the National Academy of Engineering and the National Academy of Inventors. He has over 800 publications and over 60 patents.



**Tsung-Han Yang** received the MS degree in Photonics and Optoelectronics from Nation Taiwan University, Taiwan. His previous work focused on bio-sensing application of thin-film transistors. He is currently pursuing his Ph.D. degree in Electrical Engineering at ASU, with a focus on the GaN power devices and ultrawide band gap materials.



**Shuji Nakamura** is a Cree Distinguished Professor at the University of California Santa Barbara and the Co-Director of the Solid State Lighting and Energy Electronics Center. He is the 2014 Nobel Laureate in Physics for the invention of efficient blue light-emitting diodes which has enabled bright and energy-saving white light sources. He is a fellow of the U.S. National Academy of Engineering, U.S. National Academy of Inventors, and U.K. Royal Academy of Engineering. He has published over 700 journal papers and holds more than 200 U.S. patents and over 300 Japanese patents.



**Jossue Montes** received the B.S.E. (2015) and M.S. (2019) degrees in physical electronics and photonics from Arizona State University (ASU). He is currently a research associate pursuing the Ph.D. degree in electrical, computer, and energy engineering at ASU, with an emphasis on wide- and ultra-wide bandgap semiconductors.



**Fernando A. Ponce** is a Professor of Physics at Arizona State University, since 1999. His research focuses on the physics of semiconductor materials, for electronic and optoelectronic applications. He received his BS degree in Physics from the National University of Engineering (UNI) in Lima, Peru, and PhD degree in Materials Science and Engineering from Stanford University. He worked at Hewlett-Packard Laboratories in Palo Alto, California (1980–1984), and at the Xerox Palo Alto Research Center (1977–1980, 1984–1998). His current interest is in the understanding of materials properties of III-nitrides, and their correlation to growth parameters and device performance. He is a fellow of the Latin American Academy of Sciences, and of the American Physical Society.



**Cun-Zheng Ning** is a Professor of Electrical Engineering at Arizona State University. He received Ph.D. degree in physics from the University of Stuttgart, Germany. His current research interests are in the general area of semiconductor nano-optoelectronics including 2D materials and related devices applications; plasmonic and metallic cavity nanolasers; semiconductor nanowire materials and photonic applications, especially semiconductor alloys with largely tunable alloy compositions and bandgaps for full-spectrum solar cells and multiwavelength and white lasers. Dr. Ning is a fellow of the Optical Society, a fellow of IEEE, and a fellow of Electromagnetic Academy. He was a recipient of several awards including NASA Award on Nanotechnology and Devices and the IEEE/Photonics Society Distinguished Lecturer Award.



**Yuji Zhao** is an Assistant Professor of Electrical Engineering at Arizona State University, where his research focuses on advanced electronic and optoelectronic devices based on wide bandgap III-nitride semiconductors. He has authored/co-authored more than 150 journal and conference publications, 4 book chapters, and over 20 patents. He is a recipient of 2019 Presidential Early Career Award for Scientists and Engineers, 2019 MIT TR 35–China Award, 2017 ASU Fulton Outstanding Assistant Professor Award, 2016 DTRA Young Investigator Award, 2015 NASA Early Career Faculty Award, 2015 SFAz Bisgrove Scholar Faculty Award, and 2010–2013 UCSB SSLEC Outstanding Research Award.